
Article:
Lees, James, Durham, Ben, Anderson-Taylor, Martha et al. (4 more authors) (2023) Nanoscale Si fishbone structures for manipulating heat transport using phononic resonators for thermoelectric applications. Physica Scripta. 095928. ISSN 0031-8949

https://doi.org/10.1088/1402-4896/aced72

Nanoscale Si fishbone structures for manipulating heat transport using phononic resonators for thermoelectric applications

Physica Scripta

PAPER

Nanoscale Si fishbone structures for manipulating heat transport using phononic resonators for thermoelectric applications

James Lees, Ben Durham, Christopher Reardon, Martha Anderson-Taylor, Matt Probert, Philip Hasnip and Sarah Thompson

School of Physics, Engineering, and Technology, University of York, Heslington, YO10 5DD, United Kingdom

E-mail: James.Lees@york.ac.uk

Keywords: SThM, AFM, phononic resonance, thermoelectric, metamaterials, thermal conductivity

OPEN ACCESS

RECEIVED
7 June 2023

REVISED
26 July 2023

ACCEPTED FOR PUBLICATION
4 August 2023

PUBLISHED
16 August 2023

Abstract

Thermoelectric materials have the potential to convert waste heat into electricity, but their thermoelectric efficiency must be improved before they are effective and economically viable. One promising route to improving thermoelectric efficiency in thin-film thermoelectric materials is to reduce the material's thermal conductivity through nanopatterning the surface. In this work nanoscale phononic resonators are introduced to the surface, and their potential to reduce thermal conductivity is explored via coupled experimental and theoretical techniques. Atomistic modelling is used to predict the dependence of the thermal conductivity on different design parameters and used to guide the design and fabrication of silicon fishbone nanostructures. The nanostructure design incorporates a variation on design parameters such as barb length, width and spacing along the shaft length to enable correlation with changes in thermal conductivity. The thermal characteristics of the nanostructures are investigated experimentally using the spatial resolution of scanning thermal microscopy to correlate changes in thermal conductivity with the changes in the structure parameters. The method developed uses a microheater to establish a temperature gradient along the structure which will be affected by any local variations in thermal conductivity. The impact on the thermal gradient and consequently on the tip temperature is modelled using finite element computer simulations. Experimental changes as small as 7.5% are shown to be detectable in this way. Despite the experimental technique being shown to be able to detect thermal changes far smaller than those predicted by the modelling, no modifications of the thermal conductivity are detected. It is concluded that in order to realise the effects of phononic resonators to reduce thermal conductivity, that much smaller structures with a greater ratio of resonator to shaft will be needed.

1. Introduction

Climate change is a major worldwide challenge with a significant number of technologies being developed to improve the efficiency of energy use. Thermoelectric devices recover waste heat and turn it into useful electrical energy. However, current thermoelectric materials are not sufficiently efficient to be economically viable. Their efficiency is governed by the dimensionless 'Figure of Merit' ZT defined as:

$$ZT = \frac{S^2\sigma}{\kappa}T \tag{1}$$

where S is the Seebeck Coefficient; σ is the electrical conductivity, κ is the sum of the lattice thermal conductivity, κ_{lat}, and the electronic thermal conductivity, κ_{el}, and T is the mean temperature.

Most materials used for thermoelectric purposes have ZT values of around 0.5–1 [1]. To reach values above this, materials are being sought which have a high electrical conductivity but a low thermal conductivity, whereas these two properties are usually co-dependent.

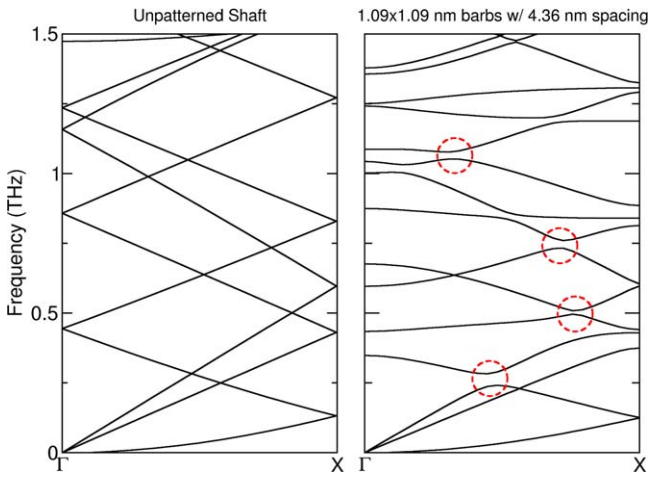

Figure 1. Comparison of the simulated low-frequency phonon dispersions of (left) a bare silicon membrane and (right) a membrane with additional surface nanostructures. The group velocity is the gradient of the dispersion curve, and the modes for the nanostructured membrane show clear regions of very low group velocity (flat modes; circled).

Metamaterials use their composite material and/or geometric structure to create properties not intrinsic to the original materials. Much previous work has focused on reducing the lattice thermal conductivity of materials by increasing phonon scattering [2]. However, this tends to also increase the scattering of the charge carriers and thus also reduce the electronic conductivity and therefore ZT.

In this work, the possibility of using nanoscale phononic resonance to modify a metamaterial device's thermal conductivity whilst leaving the σ unchanged is explored. In particular, the impact of different device parameters on the thermal conductivity is explored through simulation to guide the design of fabricated silicon metamaterial devices. The spatially resolved technique of scanning thermal microscopy (SThM) is used to allow for correlation of any thermal conductivity changes with the design parameters of the nanoresonators.

Typical thermoelectric materials are semiconductors, in which the thermal transport is dominated by phonons. In order to reduce the lattice vibrations' contribution to the thermal conductivity, κ_{lat}, the phonons need to be scattered as they travel through the material. Historically, the phonon mean free path, Λ_{ph} (and hence thermal conductivity) of thermoelectric materials has been reduced by introducing additional scatterers, such as atomic dopants, and scattering mechanisms such as grain boundaries, which reduce the scattering time [3–5]; however, these modifications can also increase the scattering of charge carriers, which leads to an undesirable decrease in σ. Over the last decade, an alternative approach has been developed in the field of nanophononics, in which the phonon dispersion itself is engineered by modifying the structure of the material on the nanoscale [6, 7]. In the case of thermoelectrics, the group velocity of the phonons is reduced by introducing local phononic resonators, whose modes hybridise with the intrinsic modes of the thermoelectric material (as shown in figure 1), an effect known to reduce thermal conductivity [8]. In this work we attempt to achieve this by nanostructuring the surface of thin-film thermoelectrics [9].

In several publications [6, 10–12] atomistic simulations have been used to investigate the effects of patterning the surface of silicon membranes/wafers with pillar or wall-like nano-structures, and predict greatly reduced lattice thermal conductivity, $\kappa_{lat,}$ compared to unpatterned membranes. The majority of these studies have focused on the nano-pillar design in which reduction in κ_{lat} has been studied as a function of the pillar's design parameters which have suggested that nano-pillars with large aspect ratio are most effective. Less attention has been given to the nano-wall design [13, 14]. The atomistic modelling tends to have been performed for structures at 300 K and is limited to small structure sizes. There are also some limitations to the simulation methods that have been used to date. Methods using the Callaway-Holland model are reliant on experimental scattering data which, given our aim is to significantly impact the phonon modes, this scattering data may no longer be applicable. Finally, the Molecular Dynamics (MD) simulations are temperature specific and suffer from finite size effects, because the finite simulation cell dimensions place upper limits on the allowed phonon wavelengths.

As well as the atomistic modelling, Nomura and Anufriev performed Finite Element Modelling (FEM) to explore a variety of device designs [15, 16] including the nano-pillar [17, 18] and nano-wall like design [9, 19, 20]. The FEM was used to study the effects of altering individual design parameters such as structure, the length and width of the walls and the thickness of the shaft, on device performance. Using FEM allows consideration of much greater length scale than is possible with the atomistic modelling, however relies on the assumption that

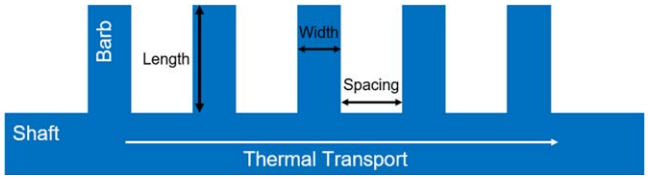

Figure 2. Schematic diagram of Si fishbones showing design parameters and form.

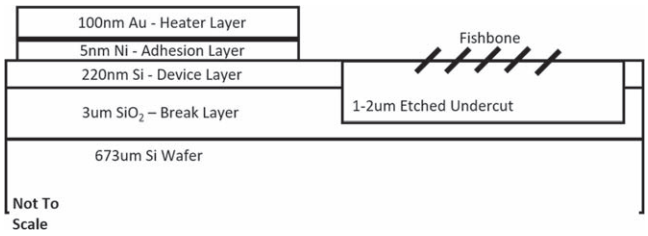

Figure 3. Schematic diagram of construction of Si fishbones.

the phonons are elastic in nature, which limits the applicability of these simulations to temperatures of less than a few Kelvin [15].

The metamaterials investigated in this work are silicon 'fishbone structures', named after the similar looking structures created by Maire *et al* [9] which resemble a fish skeleton. Our structures were designed to study the predicted κ reduction by using a series of barbs extended laterally from a central shaft which is suspended over an undercut surface allowing them to freely vibrate and specifically to enable the spatial resolution of SThM to reveal the impact of different parameters on the thermal transport. The fishbones are shown as a schematic in figure 2 and can be seen realised in silicon in the SEM image, figure 5.

The design parameters for the fishbone nanostructures are the length and width of each 'barb', and the spacing between them. The experimental results of [9] suggest that the reduction in κ_{lat} could be optimised by increasing the ratio of Length:Width. One feature of our fabrication process is that it allows for the manufacturing of devices with resonators with large length:width aspect ratios. This enabled us to test aspect ratios up to 26:1 compared to previous studies where the largest length:width aspect ratio manufactured or modelled is ~2.5:1 [9, 14, 19, 20].

In order to detect correlations between the barb parameters and the thermal conductivity, κ, of these devices, a thermal gradient was established along the shaft of the fishbone and its spatial variation measured using SThM. By using an atomistic forcefield to model forces between atoms, we solve the Boltzmann Transport equation (BTE) to predict the trends in κ_{lat} 'fishbone' nanostructures across a range of aspect ratios. The predicted trends were then compared to experimental trends found for manufactured Si devices with the same design, albeit on a different length scale. The results of the atomistic simulations were also used in continuum simulations to aid interpretation of the experimental data and establish whether the expected change in κ_{lat} of the nanostructures would be detectable by the SThM.

2. Method

2.1. Si fishbone fabrication

Fabrication of the Si fishbones was performed using silicon on insulator (SoI) chips. These had microheaters constructed on the surface using spin coating, UV lithography and metal deposition. They were constructed using a 5 nm Ni adhesion layer and a 100 nm Au heating layer which were connected to a circuit using indium wire. This could be supplied with a current to produce a thermal gradient across the sample surface.

The Si fishbones were then created on the SoI chips by spin coating and e-beam lithography to pattern the fishbones onto the sample in close proximity to the microheaters. A reactive ion etch comprising a gas mixture of 1:1.2 CHF_3 to SF_6 was then used to cut out the fishbone pattern and the chip was then wet etched using HF which resulted in the undercut Si fishbones as shown in figure 3.

Table 1. Design parameters for each set of simulation cells. The varied parameter is shown in bold with its minimum value and maximum value. The final column gives the step length in the varied parameter between the min and max values.

Set	Length (nm)	Width (nm)	Spacing (nm)	Step (nm)	Length : width ratio
1	**1.09–4.36**	1.09	1.09	1.09	**1:1–4:1**
2	1.63	**1.09–2.72**	1.09	0.543	**3:2–3:5**
3	1.09	1.09	**1.09–4.36**	1.09	1:1

Silicon was chosen as whilst it is a poor thermoelectric material, the majority of its thermal conductivity comes from the phonons and hence should clearly demonstrate the effect of nanoresonators on the thermal conductivity. In addition, experimental fabrication of Si nanostructures is well understood and controlled.

2.2. Atomistic simulation

The Conventional unit Cell (CC) of silicon contains 8 atoms and is cubic with a lattice constant of 0.543 nm. Due to its cubic geometry, the CC is therefore a convenient building block for constructing the larger simulation cells of the fishbone nanostructures. Three sets of simulation cells were created so that each set varied one of the design parameters whilst keeping the others constant. The parameters varied were the length of the barbs; the width of the barbs and the spacing between the barbs, with the choice of values for these parameters given in table 1 below. The thickness of the shaft (along the y-direction of the schematic) was kept constant for all the simulations.

A large number of atoms per simulation is required to accurately describe the geometry of these systems. Continuing in the vein of previous simulation work [6, 10–12], we therefore make use of interatomic potentials for modelling the forces acting on/between atoms rather than more accurate methods such as Density Functional Theory (DFT). The Stillinger-Weber (SW) potential [21] and the Tersoff potential [22] are common choices of interatomic potentials when modelling silicon, both being found to give a good balance of transferability between different geometries and computational efficiency [23]. We performed simulations using both potentials to confirm that any predicted trends for the change in κ_{lat} as the design parameters are varied is independent of the choice of interatomic potential.

The predictions of the lattice thermal conductivity in this work were made by solving the phonon Boltzmann Transport equation (BTE) [24]. This was done using the ShengBTE code [25] which requires input of the 2nd and 3rd order Interatomic Force Constants (IFCs) of the system. These are the second and third derivatives of the system's total energy with respect to the atomic positions. ShengBTE uses the IFCs to calculate values for several thermal properties of the lattice, including κ_{lat}, at a range of temperatures. By including the 3rd order IFCs, ShengBTE can calculate the effects due to phonon–phonon scattering events involving one or two phonons. This reduces the model's dependence on empirical data obtained from experiments where the crystal geometry can be vastly different, but it limits the types of scattering events that are included. The advantages of this approach are that; unlike MD simulations, the BTE solution does not suffer from finite size effects and that once the scattering rates have been calculated, it is relatively fast to compute the solution at several temperatures.

The model is unable to account for scattering events due to material defects or scattering events of three or more phonons. The importance of the first issue is mitigated by the ability to manufacture very high-quality silicon samples that have relatively few defects. As temperatures increase above 500 K, higher order phonon effects become important due to the increased thermal energy in the system. At these elevated temperatures, enough phonons may be excited such that there is a high enough density of phonons in the system for 3-way phonon interactions to become a significant scattering mechanism. Due to the choice of using the interatomic potentials, there is also no way to include predicted electron–phonon scattering events within the model. It should therefore be expected that any prediction of κ_{lat} would be an overestimation, especially at higher temperatures where the 3-way phonon–phonon scattering events will become significant. This overestimation of κ_{lat} will however occur for all systems considered and so predictions of relative changes in κ_{lat} due to changes to the systems can still be made with robustness.

The size of nanostructures that can be investigated in this manner is limited by the number of atoms required in the primitive unit cell. The time required to solve the BTE scales with the number of atoms in the primitive cell, N_{at}, as $O(N_{at}^6)$. This limits the size of the primitive cell that can be used, since above ~300 atoms the solution of the BTE takes impractically long to compute. One advantage of using the BTE over a molecular dynamics (MD) method, is that once the phonon–phonon scattering matrix has been calculated, ShengBTE can very quickly determine values of κ_{lat} for several temperatures, whereas MD methods require a full repetition of the simulation at each temperature. Understanding the performance of these devices at different temperatures is particularly useful for a thermoelectric application.

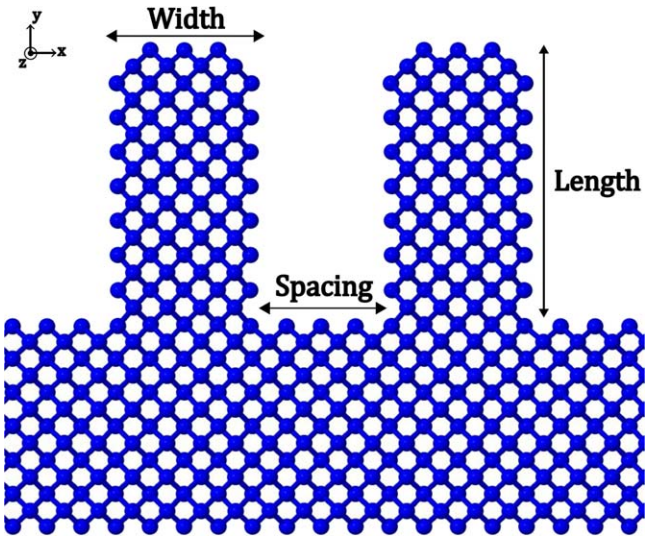

Figure 4. Atomic configuration used for the nanostructure simulations with each of the varied design parameters.

The 2nd and 3rd order IFCs were calculated via the finite-displacement method with the materials modelling code CASTEP [26]. CASTEP can calculate the 2nd order IFCs directly using a non-diagonal supercell method [27] and use them to plot phonon band structures. CASTEP is a DFT modelling software, but it can also use interatomic potentials via a native SW implementation and through its interface to QUIP, an interatomic potential library [28]. In order to calculate the 3rd order IFCs, CASTEP has an interface to the ShengBTE package which determines the symmetry reduced set of 3rd order IFCs and generates a set of input files to perform the necessary calculations to generate them. A cut-off radius must also be provided, beyond which ShengBTE assumes that the 3rd order IFCs are zero. The SW and Tersoff potential also have an interaction cut-off radius, r_{cut}, beyond which atoms are treated as non-interacting and the interatomic forces are set to zero. However, being 3-body interatomic potentials, this means any pair of atoms within a radius $r < 2r_{cut}$ of each other could have non-zero 3rd order IFCs. Due to the number of atoms in our nano-structure simulations, including all atomic interactions within a radius $r < 2r_{cut}$ would lead to an enormous number of computations. However, in practice, it was found that beyond the second Nearest atomic Neighbours (2nd NNs) the 3rd order IFCs were negligible and had no effect on the result for κ_{lat}. This is because the interaction strength in both the SW and Tersoff potentials decays exponentially to zero as r approaches r_{cut}.

For both the 2nd and 3rd order IFCs, we need to consider phonon modes of different wavelengths, including those with wavelengths longer than the primitive simulation cell (the smallest unit cell that can be used to represent the full system). In order to capture these phonon modes, it is necessary to perform the IFC calculations using supercells of the primitive cell. Due to the choice of using interatomic potentials, we know that the IFC matrices are guaranteed to be zero beyond a certain point, which allows us to use a rather small supercell size, equivalent to a $2 \times 2 \times 1$ q-point grid sampling which still includes all non-zero IFCs. With all the non-zero IFC values, ShengBTE can use Fourier interpolation to calculate the phonon modes on a finer q-point grid, thereby including a greater range of phonon–phonon scattering events.

CASTEP uses periodic boundary conditions in all directions for its simulation cells. This requires the simulation cell to be padded with vacuum along the y-direction of the schematic shown in figure 4 such that the fishbone structure is separated from its periodic image and does not interact with itself. This vacuum gap only has to be larger than the interatomic potential cut-off to prevent interactions between the periodic images of the simulation cell. A vacuum gap of 1.09 nm (width of 2 CCs) between the tip of the nanostructure and the periodic repeat of the membrane was therefore used.

ShengBTE calculates a lattice thermal conductivity tensor for the system. From this computed tensor we take the component that describes the transport along the shaft, i.e. the *xx* component. Each value of the κ_{lat} tensor determined by ShengBTE is normalised internally simply by dividing by the cross-sectional area of the simulation cell perpendicular to the lattice direction for that component. This is not applicable for a non-bulk material simulation cell such as the fishbone nanostructures since this area includes the vacuum gap between the periodic images and the length of the barb. Therefore when calculations of κ_{lat} are performed, a correction must be applied to the value produced by ShengBTE to use the cross-sectional area of the shaft, not the full unit cell. The area that should be used to compute exact κ_{lat} is debatable as it is hard to define what the thickness of the shaft is along the *z*-axis. It is not simply the area defined by the most extreme centre positions of the atoms since

the actual atoms include electrons, which extend a radius around the position of the atom. There is also the displacement of the atoms to consider, making it difficult to appropriately gauge what thickness ought to be used. However, given all the simulation cells use the same shaft thickness of 1.63 nm (3 CCs of silicon), the relative reduction in κ_{lat} due to the introduction of the nanostructures can be accurately calculated without the 'correct' value for the shaft thickness by using a consistent value for all results. We therefore compare κ_r for each structure, where κ_r is the area corrected κ_{lat} value for the nanostructured shaft, κ_{struct}, over the area corrected κ_{lat} value of the unstructured shaft or membrane, κ_{mem}. κ_r can then be used to compare different sets of design parameters and their effect on the κ_{lat} of the shaft.

2.3. Scanning thermal microscopy

Scanning thermal microscopes are a modification of basic AFM techniques [29]. In this instance a KNT-SThM-2an [30] probe with a Pd coated tip was used in a NanoScan VLS-80 which had been converted for use as an SThM using a custom tip holder and an electronics system designed by the group of Professor Oleg Kolosov from Lancaster University, UK. A change of tip temperature causes a change in the electrical resistance of the tip which is then measurable through the use of an electronic bridge circuit. The current passed through the tip also heats it via Joule heating so that the tip can also be used as a heat source. Note that this method is optimised for measuring changes in temperature rather than absolute temperature.

The recorded tip temperature will change due to any change to the tip/sample heat flow. This has three main factors: the temperature of the surface, the thermal properties of the surface and the thermal contact resistance. The spatial variations in tip temperature are therefore directly related to spatial variations in thermal transport properties close to the surface. However, due to the contact area being a significant factor, topographical features can also cause a detectable change in the thermal signal as the changing tip/sample contact will result in a corresponding change in solid–solid contact area.

In order to examine any potential changes in the thermal conductivity, a thermal gradient was applied across the fishbone. An altered thermal conductivity will result in an altered thermal gradient that can be measured using SThM.

2.4. COMSOL finite element modelling

COMSOL [31] modelling of the SThM tip temperature along the shaft was also performed. This model did not have the capabilities to calculate any kind of phononic phenomena but was used to simulate the effects that a changing thermal conductivity across a fishbone shaft would have on the temperature of the shaft and the measured tip temperature.

The model used a Joule heated tip which scanned over the surface of the Si shaft which had been assigned areas of different thermal conductivity. This allowed the change of temperature of the tip to be simulated.

3. Results

3.1. Si fishbone fabrication

Silicon fishbones were grown as shown in the SEM image in figure 5. All fishbones used in the examinations had a central shaft length of 26 μm and width of 1 μm and all barbs had a width of 115 nm. The other parameters were varied during experimentation.

The central shaft membrane is examinable using the SThM tip allowing study of variations in the thermal conductivity with spatial resolution via measurement of the variation in a temperature gradient established along the shaft. The thermal conductivity of the central shaft is expected to change due to the parameters of the barbs, so in order to be able to detect a change in the thermal conductivity along a single fishbone, Multi-Aspect Ratio Fishbones (MARFs) and Multi-Density Fishbones (MDFs) were developed. As shown in figure 6 these incorporate a change in the barb parameters (barb length and barb spacing respectively) at the halfway point along the fishbone shaft. The MARFs were all constructed using one half with a 9:1 aspect ratio and the other side at values ranging between 2:1 and 26:1. The MDFs had a period between barbs of between 300 nm and 2000 nm on one half with 700 nm on the other which equates to an aspect ratio of 9:1.

Reliability of fishbone construction was good below an aspect ratio of 10:1. Above this an increasing number of barbs would stick together and at more extreme lengths could sag and make contact with the undercut surface. For the experimental study, only those fishbones where this effect was not seen were chosen.

It was also found that the surface surrounding the undercut Si surface was sometimes raised in a bubble shape around the fishbone. This resulted in the central shaft being curved upwards as shown in figure 7.

This occurs due to inherent stress within the device silicon layer. During the undercut process, some over-etching occurs into the surrounding SiO_2, this releases some of the device silicon above it which is pulled upwards by the material stress as shown in figure 8.

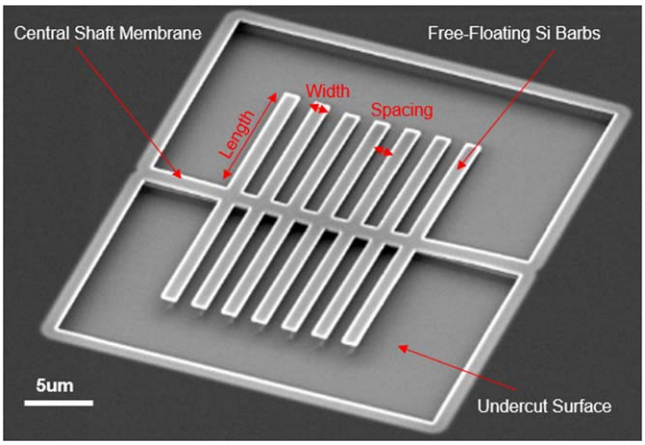

Figure 5. SEM image of a suspended silicon fishbone with components labelled.

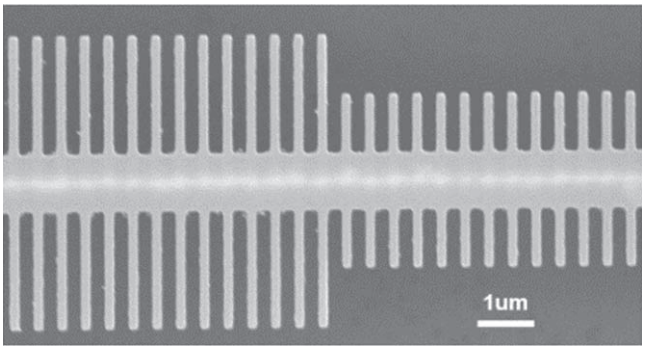

Figure 6. SEM image of MARF fishbone showing two sets of barbs with different heights on a single shaft. The two regions are labelled $\kappa 2$ (Left) and $\kappa 3$ (Right) where $\kappa 1$ and 4 are the regions either side without barbs.

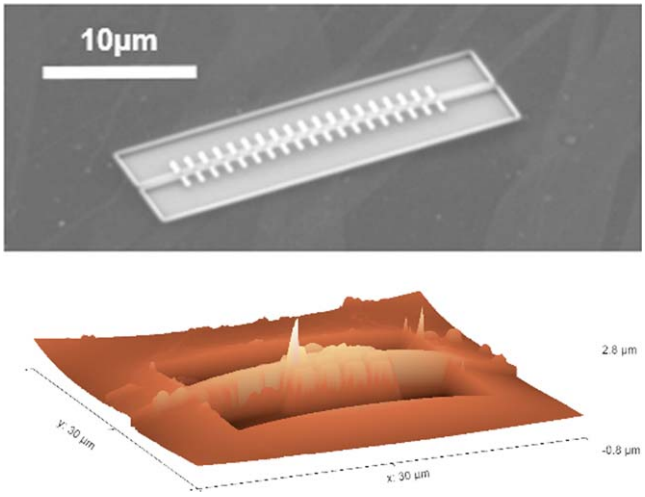

Figure 7. SEM Image showing fishbone bowing (Top) and AFM topography image showing fishbone bowing and surface bubbling (Bottom).

The degree of over-etching that occurs is due to the grain structure of the underlying SiO_2 and the length of time in the HF etch, which resulted in variations in the degree of bowing between different chips. Multiple samples were produced and those with the least bowing (<100 nm change across length of shaft) were selected for measurement.

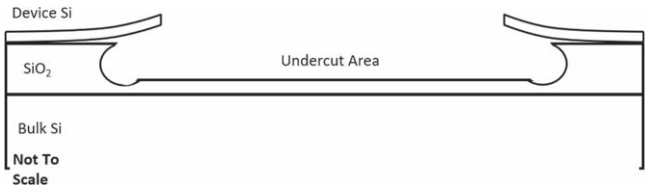

Figure 8. Diagram of anisotropic over-etching by HF which results in undercut device Si which then causes surface bubbling and shaft bowing.

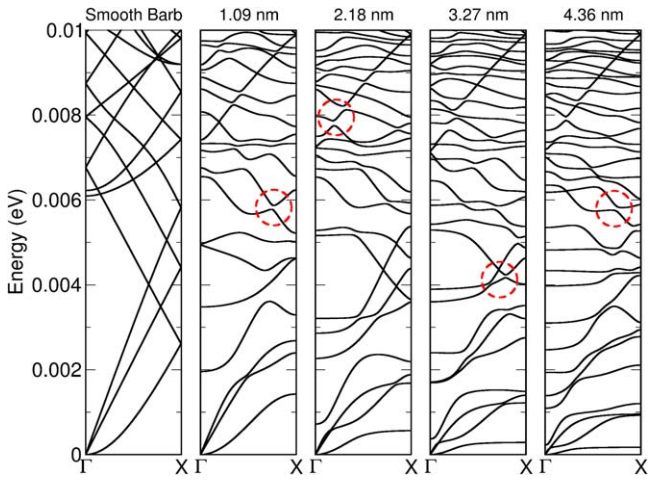

Figure 9. Comparison of the SW phonon dispersions for the low energy phonon modes for a shaft with barbs of increasing length (Set 1) at 0 K. Areas where hybridisation of phonon modes can be seen are highlighted.

It should also be noted that the ion etching process which created the barbs was found to over-etch in an advantageous way. This resulted in the fabrication parameters for the width of the barbs being set at 200 nm but over-etching resulted in ~115 nm. This resulted in an increase in the aspect ratio of the barbs (for example 15:1 became 26:1), but a reduction in the density of the barbs.

The microheaters were provided with a voltage which could be increased up to 6V. This resulted in a maximum thermal gradient across the length of the fishbone shafts of 2.7 ± 0.02 mK μm^{-1}.

3.2. Atomistic simulation

Figure 9 shows plots of the predicted phonon band structure (calculated with the SW potential) along the direction of thermal transport, i.e. along the shaft of the fishbone at 0 K. The figure shows how the band structure is predicted to vary as the length of the fishbone barb is increased. As can be seen, several low frequency modes are introduced which can be seen to hybridise with modes of the shaft such that the group velocity (gradient across the phonon BZ) is greatly reduced for many of the phonon modes. As the length of the barb increases, it can be seen that more modes become hybridised, which can indicate a reduction in κ_{lat}.

The predicted reduction in κ_{lat} due to barbs of increasing length is shown in figure 10 by plotting the ratio (κ_r) of the thermal conductivity of the barbed nanostructure (κ_{struct}) to that of the bare membrane (κ_{mem}). Here we show the results for the SW and Tersoff potentials with complete IFCs sets which were converged with respect to the interpolated q-point to within 5% of the final value for κ_{lat}. Also shown are the results using the SW potential where the 3rd order IFCs were only computed for the 1st nearest atomic neighbours and using a coarser q-point mesh. It can be seen that both SW and Tersoff (when fully converged) predict the same trend in the reduction of κ_{lat}, i.e. as the length of the barb is increased, κ_{lat} reduces further. Although the two models differ in the precise reduction, the trend is the same. This trend is also seen in the under-converged SW calculations, which are orders of magnitude faster to compute than the fully converged calculations. We therefore chose to use SW with lower convergence tolerances for the subsequent calculations to test the trends in κ_r as the other design parameters were altered.

From the values of κ_r, shown in figure 11(a), calculated for fishbone nano-structures, it was found that increasing the length of the barbs resulted in shafts that had the greatest reduction in κ_r. Increasing the width of the barbs also improves the reduction of κ_r however the effect is less marked, therefore precedence should be

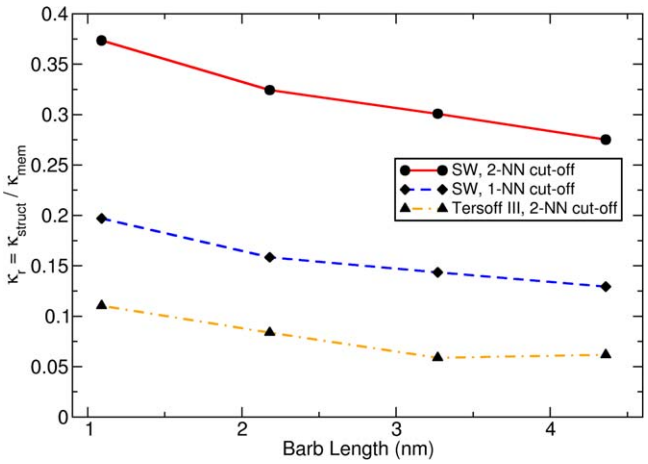

Figure 10. The relative reduction in thermal conductivity κ_r at 300 K as a function of barb length for the SW and Tersoff models. The red and orange lines represent the converged results for the SW and Tersoff models, both using a q-point grid of $4 \times 16 \times 1$. The blue line shows the trend of SW with an under converged q-point grid of $2 \times 8 \times 1$ and with a set of 3rd order IFCs which only includes the 1st nearest neighbours.

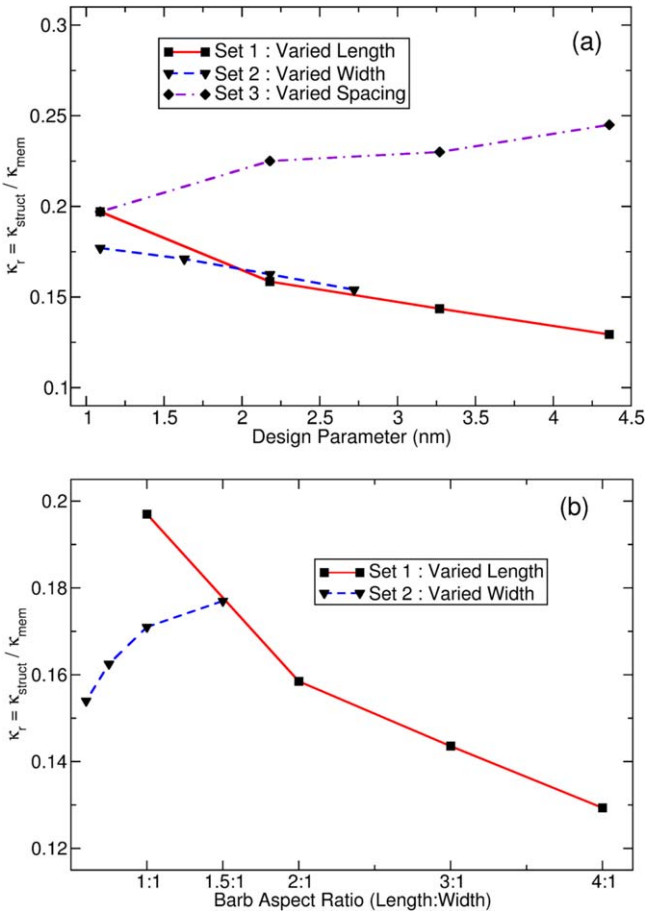

Figure 11. (a) The relative reduction in thermal conductivity, κ_r, at 300 K, as a function of the barb design parameters. (b) κ_r at 300 K as a function of the barbs length to width aspect ratio.

given to taller, thinner barb designs over wider, shorter designs. The predictions also suggest that increasing the spacing between the barbs causes an increase in κ_{lat}. Figure 11(b) plots the variation of κ_r with aspect ratio showing a different dependence for Sets 1 and 2 which are different sizes. Due to the limited sample points and small size of the simulations it is difficult to extrapolate from this data to much larger aspect ratios. However, the results suggest that the optimal fishbone structure for reducing κ_{lat} will be long finely spaced barbs

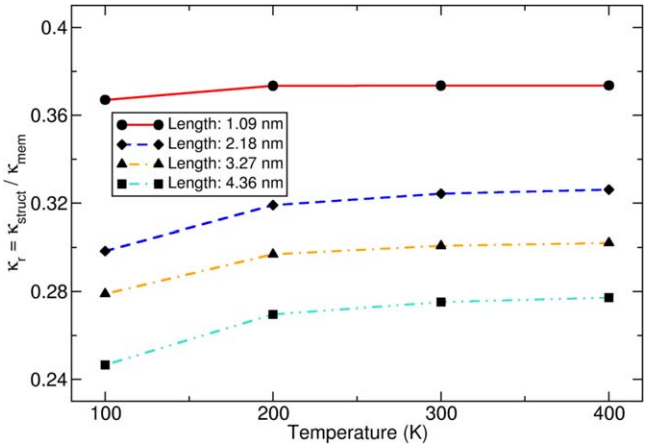

Figure 12. The relative reduction in κ_{lat} at different barb lengths as a function of temperature using Set 1 and using the SW potential with higher convergence.

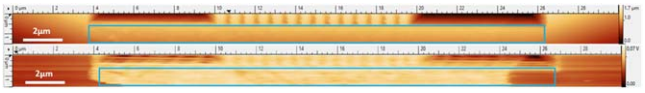

Figure 13. Representative topography (Top) and thermal (Bottom) scan images of a Si fishbone shaft used for data analysis. Blue boxes show the scan area used for shaft examinations. Note the slight shift in x direction between the two images, this is accounted for in data collection.

i.e. maximising the Length:Width ratio of the nanostructures. The experimental results of Maire *et al* [9] and the FEM published in [14] show similar trends to those found in this study. Testing this prediction further with wider and longer barbs using these atomistic simulations is impractical due to the time scaling of the ShengBTE calculation.

Figure 12 shows how temperature affects κ_r. These results were obtained using the SW potential with the higher convergence tolerance parameters shown in figure 10. It can be seen from figure 12 that at lower temperatures the effect of introducing the nanostructures appears to have a greater effect on κ_r, i.e. κ_{lat} of the shaft is further decreased. As temperature increases, the κ_r increases slightly but plateaus as temperature increases. It can be assumed that at higher temperatures than the range chosen, predictions of κ_{lat} would be overestimated due to the neglect of higher-order phonon–phonon scattering events. To include these effects would require the calculation of 4th order IFCs or higher. The model also fails to account for other scattering events such as electron–phonon scattering and scattering due to defects in the material, besides isotopic scattering.

3.3. SThM examinations

Despite their suspended nature and small dimensions, the fishbones proved easily examinable and once protocols were established, breakages were rare. Scans were taken as shown in figure 13 with full visibility of the entire shaft. The line average across the width of the shaft was then taken and used for analysis.

Experiments were first performed on a shaft without any externally applied thermal gradient and at ambient temperature. Figure 14 shows several features typical of the SThM scans. Firstly, the area surrounding the fishbone (0–8 and 32–40 μm) shows a very large change in the topography caused by the surface bubbling. The change in topography causes a corresponding change in the thermal signal due to changes in tip-surface contact and thus heat paths. A similar change in the topography in the regions (shown between the blue lines in figure 14), where there is a shaft but no barbs, results in a further change in the thermal signal.

However, the region where the barbs are present (approximately 11–29 μm) has a small enough change in topography that it is not expected to cause a significant thermal result. Instead, the curve in the thermal signal is a result of reduced efficiency of tip cooling. As the tip moves along the shaft towards the centre, the heat path to the bulk which cools the tip increases in length, cooling the tip less and resulting in it heating slightly.

It is possible to eliminate the curve in the tip measurement across the shaft by applying a high enough temperature gradient. This is because the tip goes from active mode to passive mode where the tip is heated by

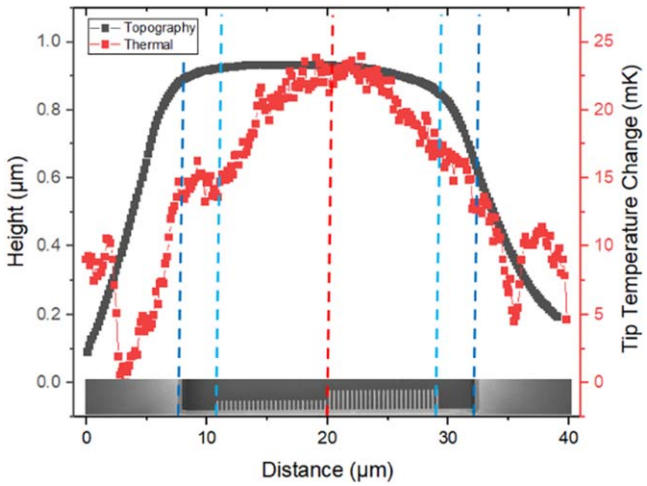

Figure 14. Comparison of topography and thermal data from a measurement of a MARF Si fishbone and surrounding area with SEM image included.

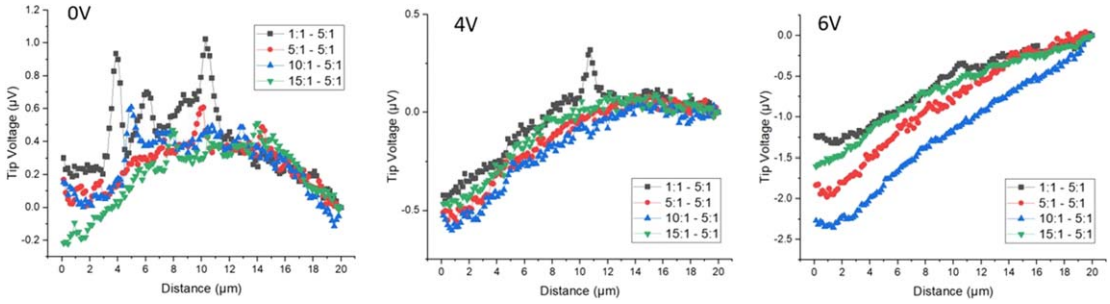

Figure 15. Tip voltage across MARF Si fishbones with different applied voltages to the microheater (i.e. increased temperature of surface) showing increased temperature reduces curve caused by tip cooling effectiveness as the tip goes from active to passive mode.

the surface rather than being cooled by it. The transition between these modes can be seen in figure 15 where the voltage applied to the microheater is increased.

Figure 16 shows measurements of the $\kappa 2$ and $\kappa 3$ regions (i.e. the suspended shaft with barbs attached where the two regions are one half of the barb pattern) for a series of MARF fishbones where there is a temperature gradient provided by the microheaters supplied with 6 V. In the $\kappa 2$ region, the aspect ratio of the barbs is varied between 2:1–26:1 by increasing their height (the width remains constant at 115 nm). The barbs remain at constant 9:1 in the $\kappa 3$ region.

The experimental results do not show evidence of a thermal gradient change at the changeover between the $\kappa 2$ and $\kappa 3$ regions which would indicate a change in thermal conductivity between the different regions of the shaft. Specifically, the recorded tip temperature does not increase as the barb's aspect ratio increases, which would be expected for a region of lower thermal conductivity. Nor are there any obvious 'breaks' at the changeover between the $\kappa 2$ and $\kappa 3$ regions. The experiments were repeated using MARF, MDF and fishbone shafts with no barbs as shown in figure 17, none of which show a clear trend or break at what would be a changeover point.

3.4. COMSOL simulations

COMSOL simulations such as those shown in figure 18 show that the change in *temperature* across the shaft of a fishbone due to a thermal conductivity change is relatively small. However, the resulting measured temperature by the SThM tip is significantly larger due to the changes in the efficiency of how the tip is cooled along the shaft. The additional heat from the tip needs to be thermalised into the bulk silicon for which the only heat path is through the shaft. This means that the SThM method can be used to find smaller thermal conductivity changes than the resulting temperature change alone might suggest.

COMSOL simulations were run where the thermal conductivity of a shaft was changed at the halfway point, splitting the shaft into three distinct regions of thermal conductivity, $\kappa 1$–3. This was designed to reflect a MARF

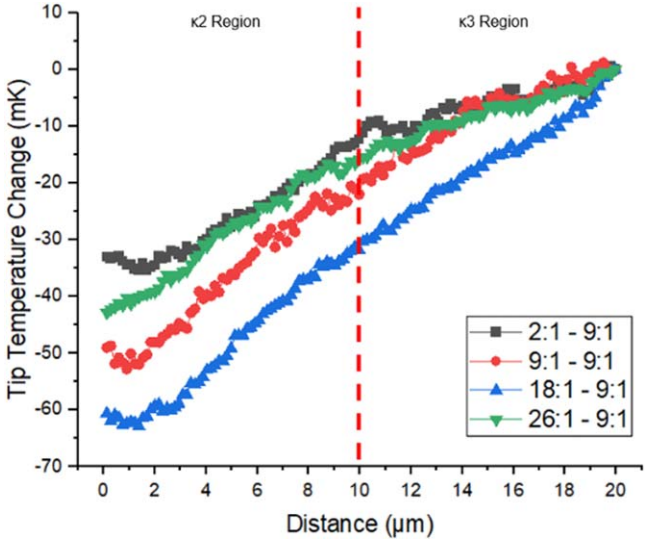

Figure 16. Line average tip temperature measurements taken across suspended Si fishbone shafts with variable barb aspect ratio.

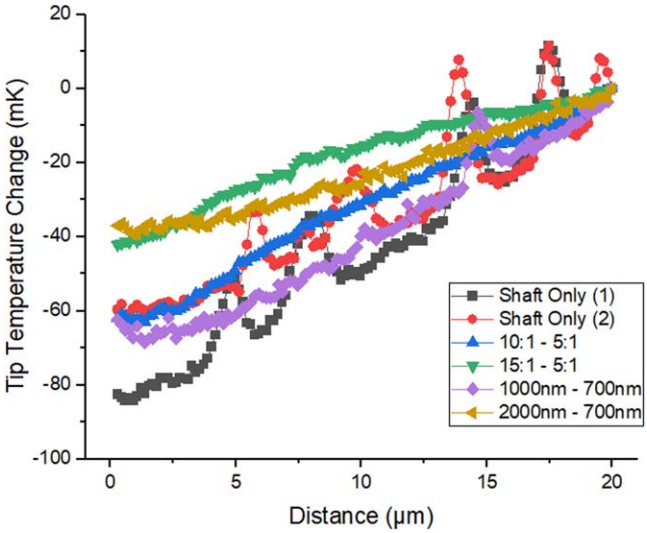

Figure 17. Line average tip temperature measurements taken across suspended Si fishbone shafts with variable barb aspect ratio, density and with no barbs present.

or MDF fishbone in which a significant difference in the thermal conductivity is predicted to be caused by the presence of barbs.

The short $\kappa 1$ regions, which are kept at a constant 100 W m.K^{-1}, are an approximation for the geometrically constricted silicon without any phononic interference. The $\kappa 3$ region represents an area with barbs which remains constant between the simulations at 85 W m.K^{-1}. The $\kappa 2$ region is the variable parameter where the thermal conductivity is varied between 50–95 W m.K^{-1} which represents a series of different length barbs having an increasing impact on K.

The results of these simulations can be seen in figure 19 which plots the tip temperature along the central line of the fishbone shaft with different thermal conductivity values. This shows that the modified thermal conductivity in the $\kappa 2$ region results in a clear overall change in the tip measured thermal gradient.

This result has a few clear features that are caused by the lowering of the thermal conductivity. Firstly, the overall temperature recorded by the tip across the $\kappa 2$ and $\kappa 3$ region was increased for a lower $\kappa 2$. Secondly, a greater difference between the $\kappa 2$ and $\kappa 3$ regions results in an increasingly distinctive 'break' in the thermal gradient.

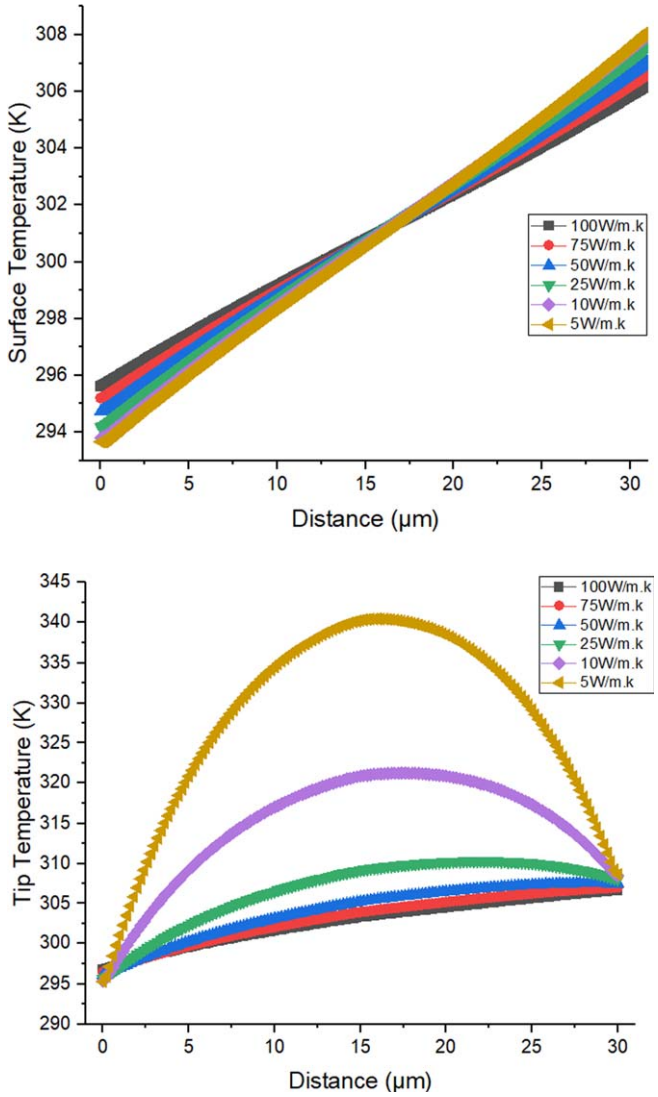

Figure 18. Comparison of simultaneous surface temperature (Top) and simulated tip temperature (Bottom) across COMSOL simulated Si fishbones for different thermal conductivity values, illustrating the effect tip cooling due to the increased thermal path at the centre of the shaft has on experimental results.

4. Discussion

As shown in figures 18 and 19, COMSOL modelling indicates that given a significant change in the thermal conductivity along the shaft, there should be a corresponding change in the tip measurement of the thermal gradient along the shaft. However, it is also clear from figures 16 and 17 that no such change was measured experimentally.

A statistical analysis of the experimental data shows that a 7.5% thermal gradient change should be detectable. The changes used in the COMSOL simulation showed a 37% change for thermal conductivity changes of 80–50 W m.K^{-1} and 28% for 80–65 W m.K^{-1}. These thermal conductivity changes are well below those suggested by the theoretical modelling which predicted approximate values of κ_r between 0.1 and 0.4. Two main possibilities for why the expected change in thermal conductivity was not seen are considered.

One possibility is that there is no significant phonon hybridisation in these fishbone nanostructures, perhaps because of insufficiently crystalline silicon, or higher-order phonon effects, which mean that the simple phonon transport theory is not directly applicable. However, Maire *et al* [9] have demonstrated a reduction in thermal conductivity with comparable nanostructure designs, although it is difficult in that work to separate the effects of dimensional reduction from the fishbone nanostructuring. It is important to note that these experiments were performed at room temperature.

The most likely explanation is that due to the scale of the structure, the effect of any hybridisation was not able to properly affect the central shaft. This could be for a number of reasons. Firstly it is not clear how well the theory scales from the ~10 nm sized atomistic models to the several μm physical structure. Whilst the modelling

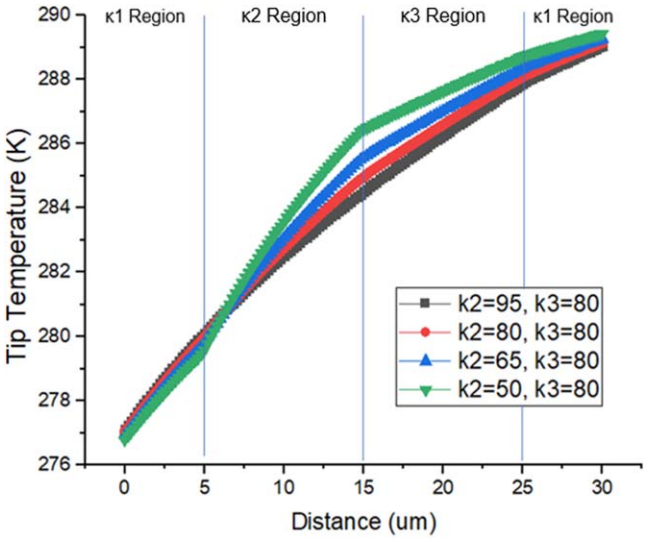

Figure 19. COMSOL results of a suspended Si shaft with different regions of thermal conductivity designed to simulate a fishbone with a significant effect on the thermal gradient.

work suggests a very large thermal conductivity change, the small size of the modelled system (at only several nm) means that not only is it made largely of surface silicon but that the addition of a barb increased the volume and surface area of the model by a more significant amount than in practice. Much of the other previous modelling work by others [6] has also used structures of a size that is not possible to reach using this fabrication method. The key difference between these structures and those which have been experimentally measured previously [9] is that the central shaft is significantly (up to 20x) wider.

A further consideration is the mean free path of the silicon. The hybridisation effect relies on the phonons retaining their coherency. However, this coherency is lost after several phonon collisions and therefore over a distance of several mean free lengths. Whilst this would not be an issue for the standard phonon mean free length in silicon (3 μm), it is known that the mean free path can be reduced in structures with restricted dimensions [32]. The length of the mean free path of the phonons within these structures is not known, and it could be that it has become short enough to effectively remove any hybridisation or localising the effect to such a degree that only a small part of the shaft is affected. Work has been performed by Anufriev *et al* [33] in which no statistically significant thermal conductivity is found and similarly, they are also unable to identify the exact reason as to why this is the case.

Throughout this work, care has been taken to simulate the thermal conductivities at comparable temperatures to the experimental measurements (room temperature). In order to perform these simulations, the harmonic phonon calculations are performed at zero temperature, and the modes populated with the appropriate thermal distribution. Whilst the CASTEP phonons are purely harmonic, some anharmonic effects are included by multiple phonon scattering processes within ShengBTE, and so this approach should be appropriate at room temperatures and below. We further assume that the phonon lifetimes are governed by the third-order (phonon–phonon) interaction, assuming that higher-order effects are negligible.

5. Conclusion

The aim of this work is to explore the potential of phononic resonators to modify the thermal conductivity of metamaterials and in particular to explore the effect of different design parameters. In common with other works, our atomistic modelling predicts a very clear change in the lattice thermal conductivity, κ_{lat}, of silicon membranes when barb nanostructures are introduced to the membrane surface. κ_{lat} is predicted to reduce by ~75% due to the introduction of the smallest and sparsest of the nano-structures studied. As the length, width and density of the nanostructures are independently increased, the reduction in κ_{lat} is predicted to increase. These trends are also predicted to persist up to and above room temperature. The precise reduction in κ_{lat} varies slightly with the choice of interatomic potential and how well converged the calculations are, but the trends in κ_{lat} as the barb design is altered remain the same. Due to the variance between the models and the use of under-converged calculations, the predicted reduction in κ_{lat} of 75% is not expected to be physically accurate. However, the fully converged SW and Tersoff potentials both predicted the same decreasing trend in κ_{lat} as the barb length was increased when compared with the under-converged (and therefore computationally much

cheaper) SW calculations. We would therefore expect the trends in κ_{lat} to be similar in manufactured samples. This trend is also seen in the work of others such as the papers of Honarvar *et al* [6, 9, 14, 19].

The parameter-dependence of the atomistic modelling guided the design of silicon fishbone structures to test different barb parameters i.e. barb length, width and spacing. In order to correlate any changes in thermal conductivity with the change in barb parameters, each device was fabricated with a change in the barb parameters at the halfway point along the fishbone shaft. Multi-Aspect Ratio Fishbones were all constructed using one half with a 9:1 aspect ratio and the other side at values ranging between 2:1 and 26:1. Multi-Density Fishbones had a period between barbs of between 300 nm and 2000 nm on one half with 700 nm on the other and an aspect ratio of 9:1. The spatial resolution of SThM was then used to correlate any changes in local thermal conductivity with these structural changes.

The SThM method developed to probe the local variations in thermal conductivity used the fabrication of a microheater to establish a thermal gradient along the fishbone. SThM was then used to measure the temperature gradient along the shaft. COMSOL modelling was used to simulate the effects of changes of thermal conductivity along the shaft on the thermal gradient and on the SThM tip temperature in order to interpret the SThM results. Modest changes of thermal conductivity, compared to the atomistic simulations, were modelled: 80–50 W m.K^{-1} along the shaft is predicted to result in a 37% change in gradient and a change of 80–65 W m.K^{-1} a change of 28%. The SThM method was demonstrated to be able to detect thermal gradient changes of 7.5%, putting these kinds of predicted changes within our measurement range.

Despite the detection ability of the SThM technique to measure the effects of changes in thermal conductivity along the structures, no significant changes were detected.

We therefore conclude that if a change in thermal conductivity due to the presence of the barbs was present, then it was too small to be detected. This suggests that the impact of the phononic resonances on the thermal conductivity of these structures is not significant. The modelling predicts that the effects are greatest for a large volume of resonant barbs compared to the membrane, suggesting that smaller nanostructures with a greater proportion of resonant features will be necessary to realise these effects.

Data availability statement

The data that support the findings of this study are openly available at the following URL/DOI: https://doi.org/10.15124/0486209b-414b-4c9b-84b2-974ca8ef5ae5.

ORCID iDs

James Lees https://orcid.org/0000-0001-8566-3935
Matt Probert https://orcid.org/0000-0002-1130-9316
Philip Hasnip https://orcid.org/0000-0002-4314-4093

References

[1] Vaqueiro P and Powell A V 2010 Recent developments in nanostructured materials for high-performance thermoelectrics *J. Mater. Chem.* **20** 9577–84
[2] Wang S *et al* 2017 Grain boundary scattering effects on mobilities in p-type polycrystalline SnSe *J. Mater. Chem. C Mater.* **5** 10191–200
[3] Uchida N *et al* 2013 Heavily doped silicon and nickel silicide nanocrystal composite films with enhanced thermoelectric efficiency *Journal of Applied Physics 7* **114** 134311
[4] Wu F *et al* 2017 Thermoelectric properties of I-doped n-type Bi_2Te_3-based material prepared by hydrothermal and subsequent hot pressing *Progress in Natural Science: Materials International* **27** 203–7
[5] Naydenov G G A *et al* 2019 Huge power factor in p-type half-heusler alloys NbFeSb and TaFeSb *J. Phys.: Mater.* **2** 035002
[6] Honarvar H and Hussein M I 2016 Spectral energy analysis of locally resonant nanophononic metamaterials by molecular simulations *Phys. Rev.* B **93** 081412
[7] Jin Y *et al* 2021 Physics of surface vibrational resonances: pillared phononic crystals, metamaterials, and metasurfaces *Rep. Prog. Phys.* **84** 0865
[8] Li W, Carrete J, Madsen G K H and Mingo N 2016 Influence of the optical-acoustic phonon hybridization on phonon scattering and thermal conductivity *Phys. Rev.* B **93** 205203
[9] Maire J, Anufriev R, Hori T, Shiomi J, Volz S and Nomura M 2018 Thermal conductivity reduction in silicon fishbone nanowires *Sci Rep.* **8** 4452
[10] Iskandar A *et al* 2016 Modification of the phonon spectrum of bulk Si through surface nanostructuring *J. Appl. Phys.* **120** 095106
[11] Wei Z, Yang J, Bi K and Chen Y 2015 Phonon transport properties in pillared silicon film *J. Appl. Phys.* **118** 155103
[12] Wei Z, Wehmeyer G, Dames C and Chen Y 2016 Geometric tuning of thermal conductivity in three-dimensional anisotropic phononic crystals *Nanoscale* **8** 16612–20
[13] Hussein M I, Leamy M J and Ruzzene M 2014 Dynamics of phononic materials and structures: historical origins, recent progress, and future outlook *Appl. Mech. Rev.* **66** 040802

[14] Yang L, Zhao Y, Zhang Q, Yang J and Li D 2019 Thermal transport through fishbone silicon nanoribbons: unraveling the role of Sharvin resistance *Nanoscale* **11** 8196–203
[15] Anufriev R and Nomura M 2016 Reduction of thermal conductance by coherent phonon scattering in two-dimensional phononic crystals of different lattice types *Phys. Rev.* B **93** 0454
[16] Nomura M *et al* 2022 Review of thermal transport in phononic crystals *Mater. Today Phys.* **22** 100613
[17] Anufriev R and Nomura M 2017 Heat conduction engineering in pillar-based phononic crystals *Phys. Rev.* B **95** 155432
[18] Anufriev R and Nomura M 2018 Phonon and heat transport control using pillar-based phononic crystals *Sci. Technol. Adv. Mater.* **19** 863–70
[19] Anufriev R and Nomura M 2019 Coherent thermal conduction in silicon nanowires with periodic wings *Nanomaterials.* **9** 142
[20] Anufriev R, Maire J and Nomura M 2021 Review of coherent phonon and heat transport control in one-dimensional phononic crystals at nanoscale *APL Mater 1* **9** 070701
[21] Stillinger F H and Weber T A 1985 Computer simulation of local order in condensed phases of silicon *Phys. Rev.* B **31** 5262
[22] Tersoff J 1989 Modeling solid-state chemistry: interatomic potentials for multicomponent systems *Phys. Rev.* B **38** 9902
[23] Michelin J v, Gonçalves L G V and Rino J P 2019 On the transferability of interaction potentials for condensed phases of silicon *J. Mol. Liq.* **285** 488–99
[24] Omini M and Sparavigna A 1995 An iterative approach to the phonon boltzmann equation in the theory of thermal conductivity *Physica B Condens Matter.* **212** 101–12
[25] Li W, Carrete J, Katcho N A and Mingo N 2014 ShengBTE: a solver of the boltzmann transport equation for phonons *Comput. Phys. Commun.* **185** 1747–58
[26] Clark S J *et al* 2005 First principles methods using CASTEP *Z. Kristallogr.* **220** 567–70
[27] Lloyd-Williams J H and Monserrat B 2015 Lattice dynamics and electron–phonon coupling calculations using nondiagonal supercells *Phys. Rev. B Condens. Matter Mater. Phys.* **92** 184301
[28] QUIP and quippy documentation — quippy bebe718 documentation [Internet]. Available from: http://libatoms.github.io/QUIP/ 07/06/2023
[29] Majumdar A 1999 Scanning thermal microscopy *Annu. Rev. Mater. Sci.* **29** 505–85
[30] Gomès S and Consortium Q H 2017 QUANTIHEAT project: main results and products *International Workshop on Thermal Investigations of ICs and Systems. Institute of Electrical and Electronics Engineers Inc.* **2017** 1–6 In: THERMINIC - 23rd
[31] COMSOL - Software for Multiphysics Simulation [Internet]. Available from: https://comsol.com/ 07/06/2023
[32] Jeong C, Datta S and Lundstrom M 2012 Thermal conductivity of bulk and thin-film silicon: a landauer approach *J. Appl. Phys.* **111** 093708
[33] Roman A and Daisuke O 2023 Impact of nanopillars on phonon dispersion and thermal conductivity of silicon membranes *Nanoscale* **15** 2248